Geosci. Model Dev. Discuss., 4, 457–495, 2011
www.geosci-model-dev-discuss.net/4/457/2011/
doi:10.5194/gmdd-4-457-2011

Geoscientific Model Development Discussions

The atmosphere-ocean general circulation model EMAC-MPIOM

A. Pozzer[1,2], **P. Jöckel**[2,*], **B. Kern**[2], **and H. Haak**[3]

[1]The Cyprus Institute, Energy, Environment and Water Research Center, Nicosia, Cyprus
[2]Atmospheric Chemistry Department, Max-Planck Institute for Chemistry, Mainz, Germany
[3]Ocean in the Earth System, Max-Planck Institute for Meteorology, Hamburg, Germany
[*]now at: Deutsches Zentrum für Luft- und Raumfahrt, Institut für Physik der Atmosphäre, Oberpfaffenhofen, Germany

Received: 8 February 2011 – Accepted: 22 February 2011 – Published: 4 March 2011

Correspondence to: A. Pozzer (pozzer@cyi.ac.cy)

Published by Copernicus Publications on behalf of the European Geosciences Union.

Abstract

The ECHAM/MESSy Atmospheric Chemistry (EMAC) model is coupled to the ocean general circulation model MPIOM using the Modular Earth Submodel Sytem (MESSy) interface. MPIOM is operated as a MESSy submodel, thus the need of an external coupler is avoided. The coupling method is tested for different model configurations, proving to be very flexible in terms of parallel decomposition and very well load balanced. The run time performance analysis and the simulation results are compared to those of the COSMOS (Community earth System MOdelS) climate model, using the same configurations for the atmosphere and the ocean in both model systems. It is shown that our coupling method is, for the tested conditions, approximately 10% more efficient compared to the coupling based on the OASIS (Ocean Atmosphere Sea Ice Soil, version 3) coupler. The standard (CMIP3) climate model simulations performed with EMAC-MPIOM show that the results are comparable to those of other Atmosphere-Ocean General Circulation models.

1 Introduction

Coupled atmosphere-ocean general circulation models (AO-GCMs) are essential tools in climate research. They are used to project the future climate and to study the actual state of our climate system (Houghton et al., 2001). An AO-GCM comprises an atmospheric general circulation model (A-GCM), also including a land-surface component, and an ocean model (an Ocean General Circulation Model, O-GCM), also including a sea-ice component. In addition, biogeochemical components can be added, for example, if constituent cycles, such as the carbon, sulfur or nitrogen cycle are to be studied. Historically, the different model components have been mostly developed independently, and at a later stage they have been connected to create AO-GCMs (Valcke, 2006; Sausen and Voss, 1996). However, as indicated by the Fourth Assessment Report of the Intergovernmental Panel on Climate Change (IPCC AR4), no model used

GMDD
4, 457–495, 2011

in the AR4 presented a complete and online calculation of atmospheric chemistry. The main motivation of this work is to provide such a model to the scientific community, which is indeed essential to effectively study the intricate feedbacks between atmospheric composition, element cycles and climate.

Here, a new coupling method between the ECHAM/MESSy Atmospheric Chemistry (EMAC) model, (Roeckner et al., 2006; Jöckel et al., 2006, ECHAM5 version 5.3.02) and the ocean model MPIOM (Marsland et al., 2003, version 1.3.0) is presented, with the coupling based on the Modular Earth Submodel System (MESSy2, Jöckel et al., 2010). In the present study, only the dynamical coupling will be discussed. Hence EMAC is, so far, only used as an A-GCM, i.e., all processes relevant for atmospheric chemistry included in EMAC are switched off. This first step towards including an explicit calculation of atmospheric chemistry in a climate model is needed to test the coupling, i.e., the option to exchange a large amount of data between the model components, and to maintain optimal performance of the coupled system. In Sect. 2, different coupling methods are briefly reviewed, followed (Sect. 3) by a technical description of the method used in this study. A run-time performance analysis of the model system is presented in Sect. 4, and in Sect. 5, results from EMAC-MPIOM are shown in comparison to other models and observations.

2 External and internal coupling methods

As sketched in Fig. 1, at least two different methods exist to couple the components of an a AO-GCM:

- Internal coupling: the different components of the AO-GCM are part of the same executable and share the same parallel decomposition topology. In an operator splitting approach, the different components (processes) are calculated in sequence. This implies that each task collects the required information, and performs the interpolation between the grids.

GMDD
4, 457–495, 2011

– External coupling: the different components (generally an atmosphere GCM and an ocean GCM) of the AO-GCM run as separate tasks[1], at the same time, i.e., in parallel. An additional external coupler program synchronises the different component models (w.r.t. simulation time) and organises the exchange of data between the different component models. This involves the collection of data, the interpolation between different model grids, and the redistribution of data.

External coupling is the most widely used method, e.g., by the OASIS coupler (Valcke et al., 2006; Valcke, 2006). The OASIS coupler is used, for example, in the ECHAM5/MPIOM coupled climate model of the Max Planck Institute for Meteorology (Jungclaus et al., 2007) and in the Unified Model of the Met Office (Dando, 2004). Also the Community Climate System Model (CCSM3, Collins et al., 2006) adopts a similar technique for information exchange between its different components.

Following the MESSy standard (Jöckel et al., 2005), and its modular structure, it is a natural choice to select the internal coupling method as a preferred technique to couple EMAC and MPIOM. In fact, the aim of the MESSy system is to implement the processes of the Earth System as submodels. Hence, the coupling routines have been developed as part of the MESSy infrastructure as a separate submodel (see A2O submodel below).

3 Coupling MPIOM to EMAC via the MESSy interface

3.1 MPIOM as MESSy submodel

According to the MESSy standard definition, a single time manager clocks all submodels (= processes) in an operator splitting approach. The MPIOM source code files (which require only minor modifications) are compiled and archived as a library. The

[1]task here refers to a process in the distributed memory parallelisation model, such as implemeted in the Message Passing Interface (MPI)

GMDD
4, 457–495, 2011

main program (mpiom.f90) is eliminated and substituted by a MESSy submodel interface (SMIL) module (messy_mpiom_e5.f90). This file mimics the time loop of MPIOM with the calls to the main entry points to those subroutines which calculate the ocean dynamics.

The MPIOM-library is linked to the model system, operating as a submodel core layer of the MPIOM submodel. In addition, the two model components (EMAC and MPIOM) use the same high level API (application programmers interface) to the MPI (Message Passing Interface) library. This implies that the same routines for exchanging information between the tasks are used. The new MESSy interface (Jöckel et al., 2010) introduces the concept of "representations", which we make use of here. The "representation" is a basic entity of the submodel CHANNEL, which, thanks to its API, represents a powerful tool in the MESSy interface. Since MPIOM is compiled as library, new representations for the ocean variables (2-D and 3-D fields) have been introduced, consistent with the MPIOM parallel domain decomposition (see below). Furthermore, in the CHANNEL API, each "representation" is related to the MPI API via a definition of the gathering (i.e., collecting a field from all cores) and scattering (i.e., distributing a field to all cores) subroutines. In case of the new MPIOM "representations", the original gathering and scattering subroutines from MPIOM are applied. As implication, the spatial coverage of each core is independently defined for the two AO-GCM components and constrained by the values of NPX and NPY set in the run script, both for the atmosphere and for the ocean model. In fact, both models, EMAC and MPIOM, share the same horizontal domain decomposition topology for their grid-point-space representations, in which the global model grid is subdivided into NPX times NPY subdomains (in North-South and East-West direction, respectively, for ECHAM5 and in East-West and North-South direction, respectively for MPIOM). Hence, the same task, which calculates a subdomain in the atmosphere, also calculates a subdomain in the ocean. An example is shown in Fig. 2, where possible parallel domain decompositions of EMAC and MPIOM are presented. A total of 16 tasks (4 times 4) is used, and the color indicates the task number in the atmosphere and ocean model, respectively.

GMDD
4, 457–495, 2011

Since MPIOM is implemented here as a submodel in the MESSy framework, the MESSy data transfer and export interface (submodel CHANNEL, see Jöckel et al., 2010) is automatically available for the ocean model without further modifications. This implies that no more specific output routines are required for the ocean model; moreover that the output files have the same format and contain the same meta information for both, the atmosphere and the ocean components.

3.2 The A2O submodel

As described in Sect. 3.1, the two components of the AO-GCM (EMAC and MPIOM) can run within the MESSy structure, sharing the same time manager. To exchanged the gridded information between EMAC and the MPIOM, a new submodel, named A2O, was developed. In EMAC, a quadratic Gaussian grid (corresponding to the chosen triangular spectral truncation) is used, whereas MPIOM operates on a curvilinear rotated grid. The exchanged gridded information must therefore be transformed between the different grids. Additionally, because the period between two subsequent data exchange events is generally different from the GCMs time step, the variables needed for the coupling have to be accumulated and averaged before being transformed. The accumulation process is performed at each time step, by adding the particular instantaneous value, multiplied by the GCM time step length (in seconds), to the accumulated fields. The averaging is done at a coupling time step, by dividing the accumulated fields by the coupling period (in seconds) and resetting the accumulated values to zero. This procedure also allows to change the GCMs time step and/or the coupling frequency during runtime.

The submodel A2O (Atmosphere to Ocean, and vice versa) performs the required accumulation/averaging in time and the subsequent grid-transformation. The submodel implementation is such that three different setups are possible:

- EMAC and MPIOM are completely decoupled,
- EMAC or MPIOM are one-way forced, i.e., one component delivers the boundary conditions to the other, but not vice versa,

GMDD
4, 457–495, 2011

– EMAC and MPIOM are fully coupled, i.e., the boundary conditions are mutually exchanged in both directions.

The setup is controlled by the A2O CPL-namelist, which is described in detail in the Supplement. Table 1 lists the variables required for the physical coupling.

For the interpolation the respective weights between the different model grid-points (atmospheric and oceanic) are calculated during the initialisation phase of the model (see also Sect. 3.3). This allows that any combination of grids and/or parallel decompositions can be used without additional preprocessing.

One of the main advantages of the coupling approach adopted in this study (internal coupling) is the implicit "partial" parallelisation of the coupling procedure. Generally, one problem of the coupling routines is that the required information must first be collected from the different tasks of one model component, then processed (e.g., interpolated) and finally re-distributed to the tasks of the other model component. This process requires a "gathering" of information from different tasks, a subsequent grid transformation, and a "scattering" of the results to the corresponding target tasks. This process is computationally expensive, in particular if many fields need to be exchanged (as is the chase for interactive atmosphere-ocean chemistry). In the internal coupling approach, only the "gathering" (or collection) and the grid-transformation steps are required. During the initialisation phase of the model system, each task (in any of the AO-GCM components) stores the locations (indices) and the corresponding weights required for the transformation from the global domain of the other AO-GCM component. Then, within the time integration phase, each task collects the required information from the global field of the other AO-GCM component. Thanks to this procedure, the interpolation is performed simultaneously by all tasks (without the need to scatter, i.e., distribute information) and thus increasing the coupling performance (see Sect. 4). It must, however, be noted that the new version of the OASIS coupler (Version 4.0, Valcke and Redler, 2006) is able to support point-to-point communication. This will potentially substantially increase the run-time performance of OASIS coupled parallel applications.

GMDD
4, 457–495, 2011

3.3 Grid-transformation utilising the SCRIP library

For the transformation of fields between the different grids (i.e., from the atmosphere grid to the ocean grid and vice versa), the SCRIP (Spherical Coordinate Remapping and Interpolation Package) routines (Jones, 1999) are used. These state-of-the-art transformation routines are widely used, for instance in the COSMOS model and the CCSM3 model. The SCRIP routines allow four types of transformations between two different grids:

- first- and second-order conservative remapping (in the MESSy system, only the first order is used),
- bilinear interpolation with local bilinear approximation,
- bicubic interpolation,
- inverse-distance-weighted averaging (with a user-specified number of nearest neighbour values).

The library has been embedded into the MESSy2 interface-structure as independent generic module (`messy_main_gridtrafo_scrip.f90`). For the coupling of EMAC and MPIOM presented here, this module is called by the submodel A2O. It can, however, also be used for grid-transformations by other MESSy submodels. According to the MESSy standard, the parameters used by A2O for the SCRIP library routines can be modified from their default values by changing the A2O submodel CPL-namelist (see the Supplement).

In Fig. 3, an example of a grid transformation with conservative remapping from the atmospheric grid to the oceanic grid is shown.

GMDD
4, 457–495, 2011

4 Analysis of the run-time performance

The run-time performance is a critical aspect for climate models and the coupling as such must not drastically decrease the AO-GCM execution speed. In order to evaluate the run-time performance, we compare the EMAC-MPIOM performance with that of the COSMOS-1.0.0 model. Since both models share the same components (ECHAM5 and MPIOM), differences in the achieved efficiency can be attributed to the different coupling methods.

For the comparison, we compiled and executed both model systems with the same setup on the same platform: a 64bit Linux cluster, with 24 nodes each equipped with 32 GB RAM and 2 Intel 5440 (2.83 GHz, 4 cores) processors, for a total of 8 cores per node. The Intel Fortran Compiler (version 11.1.046) together with the MPI-library mvapich2-1.2 has been used with the optimisation option `-O1` to compile both model codes. The two climate models were run with no output for one month at T31L19 resolution for the atmosphere and at GR30L40 resolution for the ocean. The radiation in the atmosphere was calculated every 2 simulation hours. In addition, the number of tasks requested in the simulation were coincident with the number of cores allocated (i.e., one task per core).

Since in COSMOS the user can distribute a given number of tasks almost arbitrarily between ECHAM5 and MPIOM (one task is always reserved for OASIS), the wall-clock-time required for one simulation with a given number of tasks is not unambiguous. To investigate the distribution of tasks for the optimum load balance, a number of test simulations are usually required for any given setup. Here, we report only the times achieved with the optimal task distribution. In contrast, EMAC-MPIOM does not require any task distribution optimisation and the simulation is performed with the maximum possible computational speed.

Three factors contribute to the differences in the model performance:

- The MESSy interface decreases the performance of EMAC in the "GCM-only mode" compared to ECHAM5 by ∼3–5%, and therefore, EMAC-MPIOM is

GMDD
4, 457–495, 2011

expected to be at least ∼3–5% slower than COSMOS (see http://www.messy-interface.org).

- EMAC-MPIOM calculates the interpolation weights during its initialisation phase, whereas COSMOS reads pre-calculated values from files. This calculation is computationally expensive and depends on the AO-GCM component resolutions and on the number of tasks selected. In fact, as seen before in Sect. 3.2, each task calculates the interpolation weights from the global domain of the other AO-GCM component, with the interpolation algorithm scanning the global domain for overlaps with the local domain. Although some limitations on the global domain are applied in the searching algorithm (hence increasing the performance for higher number of tasks), the interpolation calculations is the most expensive procedure in the EMAC-MPIOM coupling.

- The OASIS coupler requires a dedicated task to perform the grid transformations. Hence, for a very low core number, the single core used by OASIS limits the overall performance of the COSMOS model.

The total wall-clock-time required to complete the simulation of one month shows a constant bias of ∼58 s of EMAC-MPIOM compared to COSMOS. This bias is mainly caused by the calculation of the interpolation weights during the initialisation phase in the EMAC-MPIOM, as mentioned above, which requires additional time. To analyse the performances of the models, this constant bias has been removed from the data, so that only the wall-clock times of the model integration phases are investigated. In Fig. 4, the wall-clock times required to complete the integration phase of one month simulation is presented, dependent on the number of cores (= number of tasks) used. The wall-clock-time correlates very well between COSMOS and EMAC-MPIOM (see Fig. 4, $R^2 = 0.998$), showing that the model scalability is similar in both cases. Overall, the difference in the performances can be quantified by the slope of the regression line (see Fig. 4). This slope shows that EMAC-MPIOM performs the simulations approx. 10% faster (0.89 times) than COSMOS, disregarding the initialisation bias. Moreover,

GMDD
4, 457–495, 2011

given that the MESSy interface (which distinguishes EMAC in the "GCM only mode" from ECHAM5) decreases the run-time performance by $\simeq$3–5%, it is reasonable to conclude a 10% better run-time performance for our coupling method compared to the method used in COSMOS.

In general, the improvement in the performance is due to a reduction of the gather/scatter operations between the different tasks. In fact, as described in Sect. 3.2, the EMAC-MPIOM model does not perform the transformation as a separate task, but, instead, distributes the grid-transformation coefficients only once to all tasks, which then perform the interpolation only for their part of the domain.

5 Evaluation of EMAC-MPIOM

In order to test if the chosen coupling method technically works and does not deteriorate the climate of the physically coupled atmosphere-ocean system, we performed a number of standard climate simulations with EMAC-MPIOM and analysed the results. This analysis is not presented in full detail, because the dynamical components of EMAC-MPIOM (i.e., ECHAM5 and MPIOM) are the same as in the COSMOS model. Therefore, we refer to Jungclaus et al. (2007) for a detailed overview of the model climatology.

The model resolution applied here for the standard simulations is T31L19 for the atmospheric component EMAC and GR30L40 for the oceanic component MPIOM. This resolution combination is widely used to couple ECHAM5 with MPIOM, and it has been extensively tested (Jungclaus et al., 2010). Following the Coupled Model Intercomparison Project (CMIP3) recommendations, three simulations have been performed with different Greenhouse gas (GHG) forcings:

- a "preindustrial control simulation" with constant preindustrial conditions (GHG of the year 1850), hereafter refferd to as PI,
- a "climate of the 20 century" simulation (varying GHG from 1850 to 2000) hereafter referred to as TRANS, and

GMDD
4, 457–495, 2011

– a "1% yr^{-1} CO_2 increase to doubling" simulation (with other GHG of the year 1850), hereafter referred to as CO2×2.

These simulations have been chosen to represent some of the most important evaluations that can be performed for climate models of this complexity. In addition, the output from a large variety of well tested and reliable climate models can be used to evaluate the results. The series of annual values of the GHG for the TRANS simulations have been obtained from the framework of the ENSEMBLES European project and include CO_2 (Etheridge et al., 1998), CH_4 (Etheridge et al., 2002), N_2O (Machida et al., 1995) and CFCs (Walker et al., 2000).

5.1 Surface temperature

As shown by Jungclaus et al. (2007), the sea surface temperature (SST) and the sea ice are the most important variables for the determination of the atmosphere-to-ocean fluxes and of the correctness of the coupling processes.

In Fig. 5, the SST of simulation TRANS is compared to the SST from the Atmospheric Model Intercomparison Project (AMIP, Taylor et al., 2000), which is based on observations. Both datasets are averaged over the years 1960–1990. The correlation between the two datasets is high ($R^2 = 0.97$), which confirms that the model is generally correctly reproducing the observed SST.

Although the correlation is high, it is interesting to analyse the spatial differences between the AMIPII data and the TRANS simulation. In Fig. 6 the spatial distribution of the difference corresponding to the data shown in Fig. 5 is presented. The deviation from the observed values is less than 1 K in most regions over the ocean, in some regions the deviation is larger. The largest biases are located in the North Atlantic and in the Irminger and Labrador Seas in the Northwestern Atlantic. Deviations of similar magnitude, but with opposite sign are present in the Kuroshio region. Despite the low resolution applied for the simulations (T31L19 for the atmospheric model and GR30L40 for the oceanic one), these results are in line with what has been obtained

GMDD
4, 457–495, 2011

by the coupled model COSMOS (Jungclaus et al., 2007), where the biases of similar intensity are found in the same regions. Again, similarly to what has been obtained by Jungclaus et al. (2007), a warmer SST is observed at the west coasts of Africa and the Americas (see Fig. 6). This is probably due to an underestimate of stratocumulus cloud cover in the model atmosphere, which is also an issue with other models (e.g. Washington et al., 2000; Roberts et al., 2004), and possibly, an underestimation of the coastal upwelling in that region. Additionally, the cold bias in the North Atlantic SST is related to a weak meridional overturning circulation and associated heat transport. Finally, in the southern ocean, the too high SSTs near Antarctica and too low SSTs on the northern flank of the Antarctic Circumpolar Current (ACC) are mostly due to a positioning error of the ACC.

The surface temperature changes during the 20th century have been compared with model results provided for the Fourth Assessment Report of the Intergovernmental Panel on Climate Change (IPCC AR4). In Fig. 7, the global average surface temperature increase with respect to the 1960–1990 average is shown for simulation TRANS in comparison to a series of simulations by other models, which participated in the third phase of the World Climate Research Programme (WCRP) Coupled Model Intercomparison Project (CMPI3 Meehl et al., 2007). The overall increase of the surface temperature is in line with what has been obtained by other climate models of the same complexity. The global surface temperature is somewhat lower compared to those of other models of the CMIP3 database in the 1850–1880 period, while the trend observed during the 1960–1990 period is very similar for all models.

The tropical ocean seasonal mean interannual variability is shown in Fig. 8. It is known that ENSO (El Niño-Southern Oscillation) is the dominating signal of the variability in the Tropical Pacific Ocean region. Although in the East Pacific the simulated variability correlates well with the observed one (see Fig. 8), in the western Tropical Pacific, the model generates a somewhat higher interannual variability, which is absent in the observations. The cause is most probably the low resolution of the models. The ocean model, as applied here, has a curvilinear rotated grid with the lowest resolution

GMDD
4, 457–495, 2011

in the Pacific Ocean (see also AchutaRao and Sperber, 2006, and references therein for a review on ENSO simulations in climate models). Although the variability is generally higher in the model than in the observations, an ENSO signal is observed, as showed in Fig. 8. In this figure, the monthly variability of the SST is depicted for the so called ENSO region 3.4 (i.e. between 170° and 120° W and between 5° S and 5° N). The model variability is confirmed to be higher than the observed one; nevertheless, the model reproduces the correct seasonal phase of El Niño, with a peak of the SST anomaly in the boreal winter. Despite the difficulties in representing the correct interannual variability in the Pacific Ocean, in the Indian Ocean the model reproduces the observed patterns reasonably well, although again with a somewhat higher values.

5.2 Ice coverage

The correct simulation of the ice coverage is essential for climate models, due to the albedo feedback. As shown by Arzel et al. (2006) there are large differences w.r.t. sea ice coverage simulations between the models used for the IPCC AR4. Arzel et al. (2006) showed that, although the multimodel average sea ice extend may agree with the observations, differences of a factor of 2 can be found between individual model simulations. In Fig. 9 the polar sea ice coverage fractions for September and March are shown, calculated as a 1960–1990 average climatology from the TRANS simulation. In the same figure the observations are also shown (Rayner et al., 2003), averaged over the same period. In the Northern Hemisphere (NH) winter, the warm Norwegian Atlantic current is present, impeding the ice formation at the Norwegian coast. Nevertheless, the model seems to predict a too high ice coverage, especially over the Barent Shelf and at the west coast of Svalbard. At the same time the model overestimates the presence of ice around the coast of Greenland and at the coasts of Newfoundland and Labrador. The model reproduces, with better agreement, the retreat of the sea-ice during summer, with a strong reduction of the sea ice in the Barents and Kara Seas. Again, a somewhat higher ice coverage is present at the east coast of Greenland and northern Iceland. In the Antarctic, the eastern coast of the Antarctic peninsula (Weddel

GMDD
4, 457–495, 2011

Sea) is ice covered throughout the year. The model reproduces the right magnitude of the retreat of the ice during summer, although with some overestimation in the Ross Sea. During the Southern Hemisphere (SH) winter, an underestimation of the ice coverage is present at 30° E, while an overestimation occurs over the Amundsen Sea. The model results here differ to what has been obtained by Jungclaus et al. (2007), presumably because of the lower resolution of the models used here (∼ 3° average horizontal spacing compared to ∼ 1.5°).

To compare the changes of the sea ice coverage during the 20th century, the annual sea ice coverage area has been calculated from the simulations TRANS and PI and compared with the dataset by Rayner et al. (2003), which is based on observations (see Fig. 10). The simulated sea ice coverage agrees with the observations, although with an overestimation (up to ≃ 8%). In addition, the simulated interannual variability is much larger than what is observed, probably due to the low resolution of the model. Nevertheless the model is able to mimic the decrease in the sea ice area coverage observed after 1950, although with a general overestimation.

5.3 Thermohaline circulation and meridional overturning circulation

Deep water formation mainly takes place in the North Atlantic Ocean, and in the northern and southern parts of the Greenland Scotland Ridge. The correct representation of deep water formation is important for climate models, to maintain the stability of the climate over long time period. Figure 11 presents the maximum depth of convection estimated as the deepest model layer, where the diffusive vertical velocity is greater than zero. In the North Atlantic Ocean convection is present between Greenland and Newfoundland (Labrador Sea), with convection deeper than 1500 m. Although the model simulation agrees with the observations in this region (Pickart et al., 2002), a deep convection feature (which is the main region of deep water formation in the model) is present at the east coast of Newfoundland, which is clearly in contrast to the observations. The reason is a weak MOC (Meridional Overturning Circulation) which, combined with the strong presence of ice during winter in the Labrador sea

GMDD
4, 457–495, 2011

(see Fig. 9), forces the deep water formation in the model to be located further to the South than what is observed. Nevertheless, strong convective movement occurs in the Greenland and Norvegian Seas, reaching up the coast of Svalbard. This zone of deep water formation is well known and appears to be well simulated by the model. In the SH, convection occurs mainly in the Weddel Sea and Ross Sea, although small convective events occur around the Antarctic coast. The results are in line with the literature: the model, in fact, reproduces the regions of deep water formation (although with larger spatial extension) that have been identified by Marshall and Schott (1999, and references therein).

5.4 Jet streams

The jet streams are strong air currents concentrated within a narrow region in the upper troposphere. The predominant one, the polar-front jet, is associated with synoptic weather systems at mid-latitudes.

Hereafter, jet stream always refer to the polar-front jet. The adequate representation of the jet stream by a model indicates that the horizontal temperature gradient (the main cause of these thermal winds) is reproduced correctly. In Fig. 12, the results from simulation PI are compared with the NCEP/NCAR (National Centers for Environmental Prediction/National Center for Atmospheric Research) Reanalysis (Kalnay et al., 1996). The maximum zonal wind speed is reproduced well by the model, with the SH jet stream somewhat stronger than the NH jet stream ($\simeq 30$ and $\simeq 22\,\mathrm{m\,s^{-1}}$, respectively). The location of the maximum wind, however, is slightly shifted polewards by $\simeq 5^{\circ}$. The vertical position of the jet streams is also $\simeq 50\,\mathrm{hPa}$ higher than the observed one. The NH jet stream has a meridional extension which is in line with what is observed, while the simulated SH jet stream is narrower in the latitudinal direction compared to the re-analysis provided by NCEP. In fact, the averaged zonal wind speed higher than $26\,\mathrm{m\,s^{-1}}$ in the SH is located between $\simeq 40$–$30^{\circ}\,\mathrm{S}$ in the model results, while it is distributed on a larger latitudinal range ($\simeq 50$–$25^{\circ}\,\mathrm{S}$) in the NCEP re-analysis data. Finally, while the NCEP data show a change of direction between the tropical

GMDD
4, 457–495, 2011

and extratropical zonal winds, the simulation PI reproduces such features only in the lower troposphere and in the stratosphere, while in the upper troposphere (at around 200 hPa) westerly winds still dominate. Although some differences arise from the comparison, the general features of thermal winds are reproduced correctly by the model, despite the low resolution used for the atmospheric model (T31L19).

5.5 Precipitation

The representation of precipitation, being a very important climate variable, is still challenging for coupled climate models (Dai, 2006). The data from the Global Precipitation Climatology Project (GPCP, Adler et al., 2003) are used to evaluate the capability of EMAC-MPIOM in reproducing this important quantity. As for many other climate models, also the results from simulation PI show two zonal bands of high biased precipitation in the tropics, separated by a dry bias directly at the equator (see Fig. 13). These zonal bands (located over the Pacific Ocean) are persistent throughout the year and the magnitude is independent of the season. In addition, the Northern Intertropical Convergence Zone (ITCZ) is located slightly too far north compared to the observations during summer and autumn (see Fig. 14, JJA and SON), while too south during winter and spring (see Fig. 14, DJF and MAM). For boreal autumn and winter the simulation shows a distinct minimum at around 30° S, which is weaker in the observations. Finally, the model largely underestimates the precipitation over Anctartica throughout the year and in the storm track during the NH winter. This is associated with the underestimation of the sea surface temperature in these regions.

5.6 Climate sensitivity

To estimate the climate sensitivity of the coupled model EMAC-MPIOM, the results from the CO2×2 simulation are analysed. The simulation yields a global average increase of the surface temperature of 2.8 K for a doubling of CO_2. As mentioned in the IPCC AR4, the increase in the temperature for a CO_2 doubling "is likely to be in the range 2 to 4.5 °C

GMDD
4, 457–495, 2011




with a best estimate of about 3 °C". The value obtained in this study is thus in line with results from the CMIP3 multi-model dataset. For the same experiment, for example, the models ECHAM5/MPI-OM (with OASIS coupler) and INGV-SX6 show an increase of the global mean surface temperature of 3.35 K and 1.86 K, respectively. To calculate the climate sensitivity of the model, the mean radiative forcing at the tropopause (simulation CO2×2) was calculated for the years 1960–1990 as 4.0 $W m^{-2}$. This implies a climate sensitivity of the model of 0.7 $K W m^{-2}$, in line with what has been estimated by most models from the CMIP3 dataset (e.g., ECHAM5/MPI-OM, INGV-SX6, INM-CM3 and IPSL-CM4 with 0.835, 0.78, 0.52 and 1.26 $K W m^{-2}$, respectively).

6 Summary and outlook

A new coupling method between EMAC and MPIOM is presented. This coupling method builds directly on the capabilities of the MESSy interface. It is shown that the coupling approach of EMAC-MPIOM adopted in this study yields a better (by $\simeq$ 10%) run-time performance compared to the application of an external coupler. This good performance is obtained thanks to the coupling method implemented, which avoids load imbalances between the two dynamical components (ECHAM5 and MPIOM) and allows a higher throughput in exchanging information between the two AO-GCM components.

To evaluate the EMAC-MPIOM model system, we performed selected climate simulations to prove that the EMAC-MPIOM climate is neither deteriorated by the new approach, nor does the new model system produce results that differ from those of other climate models under similar conditions and forcings.

Following the MESSy philosophy, a new submodel (named A2O) was developed to control the exchange of information (coupling) between the AO-GCM components. However, since this submodel is flexibly controlled by a namelist, it can be used to convert any field present in one AO-GCM component to the other one and vice versa. Thanks to this capability, A2O can be used not only to control the physical

GMDD
4, 457–495, 2011

coupling between the two AO-GCM components, but also to exchange additional information/fields between the two domains of the AO-GCM, including physical and chemical (e.g., tracer concentrations) data. Hence, as a future model development, the ocean biogeochemistry will be included via the MESSy interface and coupled to the air chemistry submodels of EMAC, using the AIRSEA submodel previously developed (Pozzer et al., 2006). This will allow a complete interaction between the two AO-GCM domains, exchanging not only physical quantities necessary for coupling of the EMAC and MPIOM (i.e., heat, mass and momentum as shown here) but also chemical species of atmospheric or oceanic interest, leading to a significant advance towards a more detailed description of biogeochemical processes in the Earth system.

It must be finally stressed that the newly developed EMAC-MPIOM climate model will be used in future for chemical studies of the Earth system, while less focus will be given to climate change studies. In fact, the main components of EMAC-MPIOM are the same as the COSMOS model, and no additional (or different) dynamical processes have been added. On the other hand, the EMAC-MPIOM model can take full advantage of the results and expertises already present within the COSMOS community.

Supplementary material related to this article is available online at: http://www.geosci-model-dev-discuss.net/4/457/2011/gmdd-4-457-2011-supplement.pdf.

Acknowledgements. B. Kern acknowledges the financial support by the International Max Planck Research School for Atmospheric Chemistry and Physics. The authors wish to thank J. Lelieveld for the contribution and support in the preparation of this manuscript. We thank also the DEISA Consortium (www.deisa.eu), co-funded through the EU FP6 project RI-031513 and the FP7 project RI-222919, for support within the DEISA Extreme Computing Initiative. The simulations for this study have been performed in the DEISA grid. We acknowledge the modelling groups, the Program for Climate Model Diagnosis and Intercomparison (PCMDI) and the World Climate Research Programme's (WCRP) Working Group on Coupled Modelling (WAO-GCM) for their roles in making available the WCRP

GMDD
4, 457–495, 2011

Coupled Model Intercomparison Project phase 3 multi-model dataset. Support of this dataset is provided by the Office of Science, US Department of Energy. We acknowledge also the NOAA/OAR/ESRL PSD, Boulder, Colorado, USA, for providing the NCEP Reanalysis data, on their web site at http://www.esrl.noaa.gov/psd/. We acknowledge the usage of data from the ENSEMBLE project (contract number GOCE-CT-2003-505539). We acknowledge support from the European Research Council (ERC) under the C8 project. We acknowledge the ENIGMA (http://enigma.zmaw.de) network for support. We finally acknowledge the use of the Ferret program for analysis and graphics in this paper. Ferret is a product of NOAA's Pacific Marine Environmental Laboratory (information is available at http://www.ferret.noaa.gov).

The service charges for this open access publication have been covered by the Max Planck Society.

References

AchutaRao, K. and Sperber, J.: ENSO simulation in coupled ocean-atmosphere models: are the current models better?, Clim. Dynam., 27, 1–15, doi:10.1007/s00382-006-0119-7, 2006. 470

Adler, R., Huffman, G., Chang, A., Ferraro, R., Xie, P., Janowiaks, J., Rudolf, B., Schneider, U., Curtis, S., Bolvin, D., Gruber, A., and Susskind, P. A.: The Version 2 Global Precipitation Climatology Project (GPCP) Monthly Precipitation Analysis (1979–Present), J. Hydrometeorol., 4, 1147–1167, 2003. 473, 494

Arzel, O., Fichefet, T., and Goosse, H.: Sea ice evolution over the 20th and 21st centuries as simulated by current AOGCMs, Ocean Modelling, 12, 401–415, doi:10.1016/j.ocemod.2005.08.002, 2006. 470

Collins, W., Bitz, C. M., Blackmon, M. L., Bonan, G. B., Bretherton, C. S., Carton, J. A., Chang, P., Doney, S. C., Hack, J. J., Henderson, T. B., Kiehl, J. T., Large, W. G., McKenna, D. S., Santer, B. D., and Smith, R. D.: The Community Climate System Model Version 3 (CCSM3), J. Clim., 19(11), 2122–2143, 2006. 460

Dai, A.: Precipitation Characteristics in Eighteen Coupled Climate Models, J. Clim., 19, 4605–4630, doi:10.1175/JCLI3884.1, 2006. 473

Dando, P.: Unified Model Documentation Paper 0, version 3.0, available at: http://ncas-cms.nerc.ac.uk/html_umdocs/UM55_User_Guide (last access: 3 March 2011), 2004. 460

Etheridge, D., L.P., S., Langenfelds, R., Francey, R. J., Barnola, J.-M., and Morgan, V.: Historical CO_2 Records from the Law Dome DE08, DE08-2, and DSS Ice Cores, Trends: A Compendium of Data on Global Change, Carbon Dioxide Information Analysis Cente, Oak Ridge National Laboratory, US Department of Energy, Oak Ridge, Tenn., USA, available at: http://cdiac.esd.ornl.gov/trends/co2/lawdome.html, 1998. 468

Etheridge, D., L.P., S., Francey, R., and Langenfelds, R.: Historical CH_4 Records Since About 1000 AD From Ice Core Data, Trends: A Compendium of Data on Global Change. Carbon Dioxide Information Analysis Center, Oak Ridge National Laboratory, US Department of Energy, Oak Ridge, Tenn., USA, available at: http://cdiac.ornl.gov/trends/atm_meth/lawdome_meth.html, 2002. 468

Houghton, J. T., Ding, Y., Griggs, D. J., Nouger, M., van der Linden, P. J., Dai, X., Maskell, K., and Johnson, C. A.: IPCC – Climate Change 2001: The Scientific Basis, Contribution of Working Group I to the third Assessment Report of the Intergovernmental Panel on Climate Change, Cambridge University Press, 2001. 458

Jöckel, P., Sander, R., Kerkweg, A., Tost, H., and Lelieveld, J.: Technical Note: The Modular Earth Submodel System (MESSy) – a new approach towards Earth System Modeling, Atmos. Chem. Phys., 5, 433–444, doi:10.5194/acp-5-433-2005, 2005. 460

Jöckel, P., Tost, H., Pozzer, A., Brühl, C., Buchholz, J., Ganzeveld, L., Hoor, P., Kerkweg, A., Lawrence, M. G., Sander, R., Steil, B., Stiller, G., Tanarhte, M., Taraborrelli, D., van Aardenne, J., and Lelieveld, J.: The atmospheric chemistry general circulation model ECHAM5/MESSy1: consistent simulation of ozone from the surface to the mesosphere, Atmos. Chem. Phys., 6, 5067–5104, doi:10.5194/acp-6-5067-2006, 2006. 459

Jöckel, P., Kerkweg, A., Pozzer, A., Sander, R., Tost, H., Riede, H., Baumgaertner, A., Gromov, S., and Kern, B.: Development cycle 2 of the Modular Earth Submodel System (MESSy2), Geosci. Model Dev., 3, 717–752, doi:10.5194/gmd-3-717-2010, 2010. 459, 461, 462

Jones, P.: First- and Second-Order Conservative Remapping Schemes for Grids in Spherical Coordinates, Mon. Weather Rev., 127, 2204–2210, 1999. 464

Jungclaus, J. H., Keenlyside, N., Botzet, M., Haak, H., Luo, J.-J., Latif, M., Marotzke, J., Mikolajewicz, U., and Roeckner, E.: Ocean Circulation and Tropical Variability in the Coupled Model ECHAM5/MPI-OM, J. Clim., 19, 3952–3972, 2007. 460, 467, 468, 469, 471

Jungclaus, J. H., Lorenz, S. J., Timmreck, C., Reick, C. H., Brovkin, V., Six, K., Segschnei-

GMDD
4, 457–495, 2011

der, J., Giorgetta, M. A., Crowley, T. J., Pongratz, J., Krivova, N. A., Vieira, L. E., Solanki, S. K., Klocke, D., Botzet, M., Esch, M., Gayler, V., Haak, H., Raddatz, T. J., Roeckner, E., Schnur, R., Widmann, H., Claussen, M., Stevens, B., and Marotzke, J.: Climate and carbon-cycle variability over the last millennium, Climate of the Past, 6, 723–737, doi: 10.5194/cp-6-723-2010, http://www.clim-past.net/6/723/2010/, 2010. 467

Kalnay, E., Kanamitsu, M., Kistler, R., Collins, W., Deaven, D., Gandin, L., Iredell, M., Saha, S., White, G., Woollen, J., et al.: The NCEP/NCAR 40-year reanalysis project, Bulletin of the American Meteorological Society, 77, 437–471, 1996. 472

Machida, T., Nakazawa, T., Fujii, Y., Aoki, S., and Watanabe, O.: Increase in the atmospheric nitrous oxide concentration during the last 250 years, Geophys. Res. Lett., 22, 2921–2924, doi:10.1029/95GL02822, 1995. 468

Marshall, J. and Schott, F.: Open-ocean convection: Observations, theory, and models, Rev. Geophys., 37, 1–64, 1999. 472

Marsland, S., Haak, H., Jungclaus, J. H., Latif, M., and Röske, F.: The Max-Planck-Institute global ocean/sea ice model with orthogonal curvilinear coordinates, Ocean Modell., 5, 91–127, 2003. 459

Meehl, G. A., Covey, C., Delworth, T., Latif, M., Mcavaney, B., Mitchell, J. F. B., Stouffer, R. J., and Taylor, K. E.: THE WCRP CMIP3 Multimodel Dataset: A New Era in Climate Change Research, Bull. Am. Meteorol. Soc., 88, 1383–1394, doi:10.1175/BAMS-88-9-1383, 2007. 469

Pickart, R. S., Torres, D. J., and Clarke, R. A.: Hydrography of the Labrador Sea during Active Convection, J. Phys. Oceanogr., 32, 428–457, doi:10.1175/1520-0485(2002)032%3C0428:HOTLSD%3E2.0.CO;2, 2002. 471

Pozzer, A., Jöckel, P., Sander, R., Williams, J., Ganzeveld, L., and Lelieveld, J.: Technical Note: The MESSy-submodel AIRSEA calculating the air-sea exchange of chemical species, Atmos. Chem. Phys., 6, 5435–5444, doi:10.5194/acp-6-5435-2006, 2006. 475

Rayner, N. A., Parker, D., Horton, E., Folland, C., Alexander, L., Rowell, D., Kent, E., and Kaplan, A.: Global analysis of SST, sea ice and night marine air temperature since the late nineteenth century, J. Geophys. Res., 108, 4407, doi:10.1029/2002JD002670, 2003. 470, 471, 488, 489, 490, 491

Roberts, M. J., Banks, H., Gedney, N., Gregory, J., Hill, R., Mullerworth, S., Pardaens, A., Rickard, G., Thorpe, R., and Wood, R.: Impact of an Eddy-Permitting Ocean Resolution on Control and Climate Change Simulations with a Global Coupled GCM, J. Clim., 17, 3–20,

GMDD
4, 457–495, 2011

doi:10.1175/1520-0442(2004)017¡0003:IOAEOR¿2.0.CO;2, 2004. 469
Roeckner, E., Brokopf, R., Esch, M., Giorgetta, M., Hagemann, S., Kornblueh, L., Manzini, E., Schlese, U., and Schulzweida, U.: Sensitivity of simulated climate to horizontal and vertical resolution in the ECHAM5 atmosphere model, J. Clim., 19, 3771–3791, 2006. 459
Sausen, R. and Voss, R.: Part I: general strategy and application to the cyclo-stationary case, Climate Dyn., 12, 313–323, doi:10.1007/BF00231105, 1996. 458
Taylor, K., Williamson, D., and Zwiers, F.: The sea surface temperature and sea ice concentration boundary conditions for AMIP II simulations; PCMDI Report, Tech. Rep. 60, Program for Climate Model Diagnosis and Intercomparison, 2000. 468, 485, 486
Valcke, S.: OASIS3 User Guide, Technical report no. 3, CERFACS, PRISM Support Initiative, 2006. 458, 460
Valcke, S. and Redler, R.: OASIS4 User Guide, Technical report no. 4, CERFACS, PRISM Support Initiative, 2006. 463
Valcke, S., Guilyardi, E., and Larsson, C.: PRISM and ENES: A European approach to Earth system modelling, Concurrency Computat. Pract. Exper., 18(2), 231–245, 2006. 460
Walker, S. J., Weiss, R., and Salameh, P.: Reconstructed histories of the annual mean atmospheric mole fractions for the halocarbons CFC-11 CFC-12, CFC-113, and carbon tetrachloride, J. Geophys. Res., 105, 14285–14296, doi:10.1029/1999JC900273, 2000. 468
Washington, W. M., Weatherly, J. W., Meehl, G. A., Semtner, Jr., A. J., Bettge, T. W., Craig, A. P., Strand Jr., W. G., Arblaster, J., Wayland, V. B., James, R., and Zhang, Y.: Parallel climate model (PCM) control and transient simulations, Clim. Dynam., 16, 755–774, doi:10.1007/s003820000079, 2000. 469

GMDD
4, 457–495, 2011




Table 1. Variables to be exchanged by A2O.

Name	Meaning	Unit
	Atmosphere to Ocean	
AOFLTXWO	zonal wind stress over water	Pa
AOFLTYWO	meridional wind stress over water	Pa
AOFLTXIO	zonal wind stress over ice	Pa
AOFLTYIO	Meridional wind stress over ice	Pa
AOFLFRIO	solid freshwater flux	$m\,s^{-1}$
AOFLFRWO	liquid freshwater flux	$m\,s^{-1}$
AOFLRHIO	residual heat flux over ice	$W\,m^{-2}$
AOFLCHIO	conductive heat flux over ice	$W\,m^{-2}$
AOFLNHWO	net heat flux over water	$W\,m^{-2}$
AOFLSHWO	downward shortwave radiation	$W\,m^{-2}$
AOFLWSVO	10 meter wind velocity	$m\,s^{-1}$
	Ocean to Atmosphere	
THO	sea surface temperature	K
SICTHO	ice thikness	m
SICOMO	ice compactness (fraction of ice)	–
SICSNO	snow thikness	m
SOCU	zonal surface water velocity	$m\,s^{-1}$
SOCV	meridional surface water verlocity	$m\,s^{-1}$

GMDD
4, 457–495, 2011

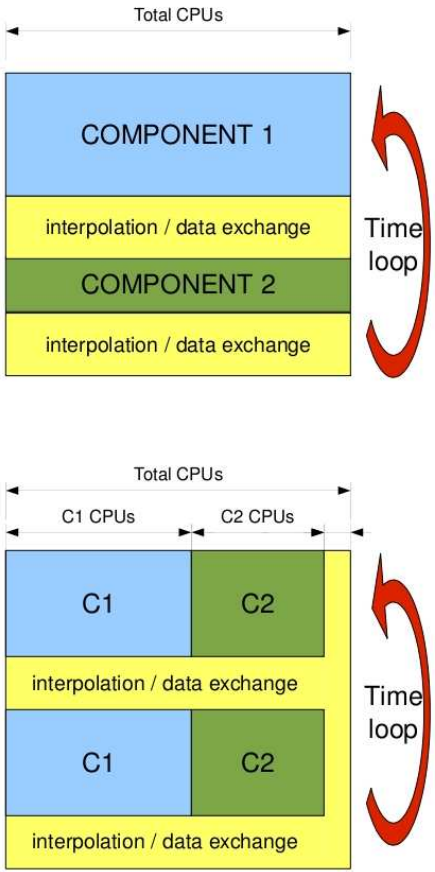

Fig. 1. Coupling methods between the different model components (C1 and C2) of an AO-GCM (upper panel “internal method”, as implemented here, lower panel ”external method” as used for example in the OASIS coupler).

GMDD
4, 457–495, 2011

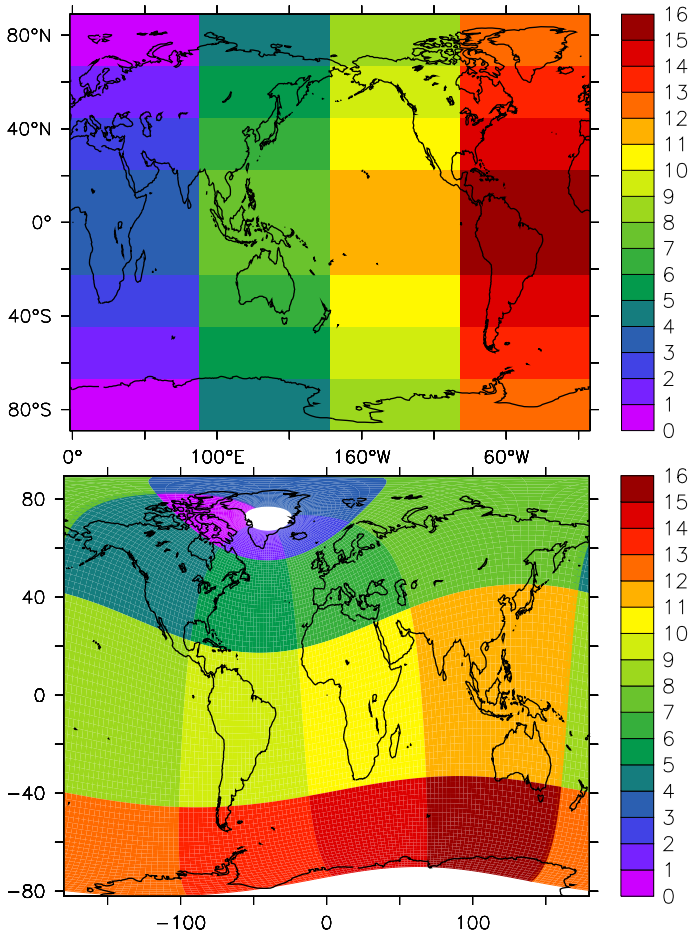

Fig. 2. Parallel (horizontal) "4 times 4" domain decomposition for a model setup with 16 tasks for the atmosphere model (upper panel) and the ocean model (lower panel). The color code denotes the task number.

GMDD
4, 457–495, 2011

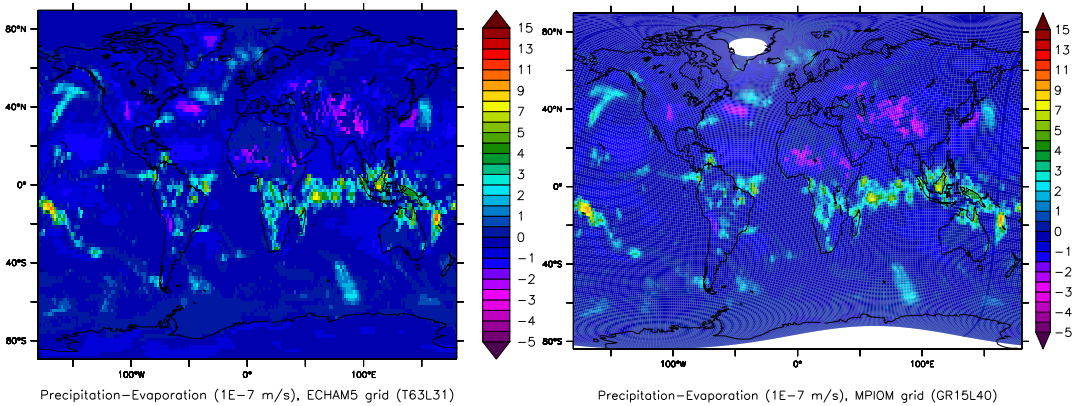

Fig. 3. Example of a grid transformation with the SCRIP library routines embedded in the generic MESSy submodel MAIN_GRIDTRAFO and called by A2O: the precipitation minus evaporation field on the EMAC grid (top) has been transformed to the MPIOM grid (bottom) using the conservative remapping.

GMDD
4, 457–495, 2011

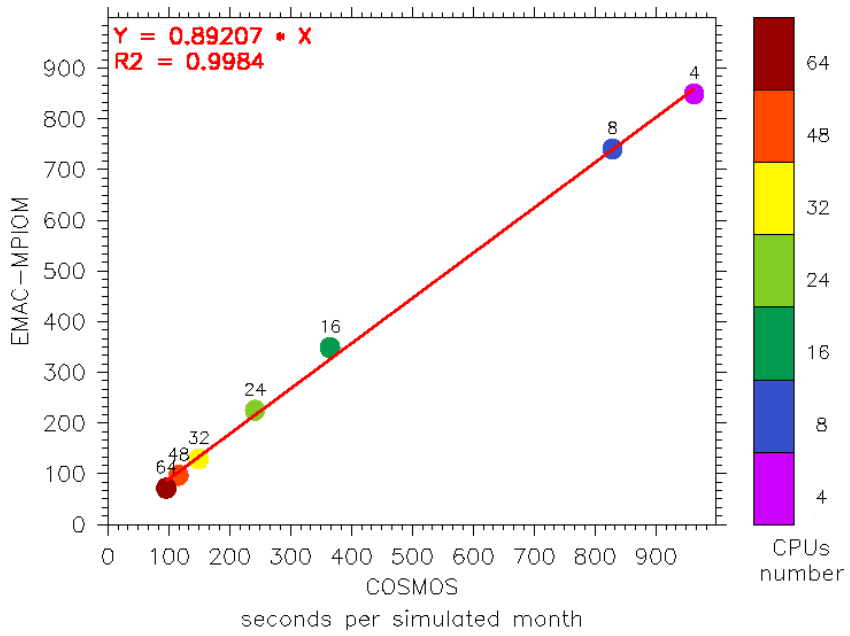

Fig. 4. Scatter plot of the time (seconds wall-clock) required to simulate one month with the COSMOS-1.0.0 model (horizontal axis) and with the EMAC-MPIOM model with the same setup. The color code denotes the number of tasks used (for clarity the number of tasks used are shown also on the top of the points). In these simulations one task per core has been used. The regression line is shown in red and the result of the linear regression is denoted in the top left side of the plot. The constant bias of 58 s, due to the longer initialisation phase in EMAC-MPIOM, has been subtracted from the data.

GMDD
4, 457–495, 2011

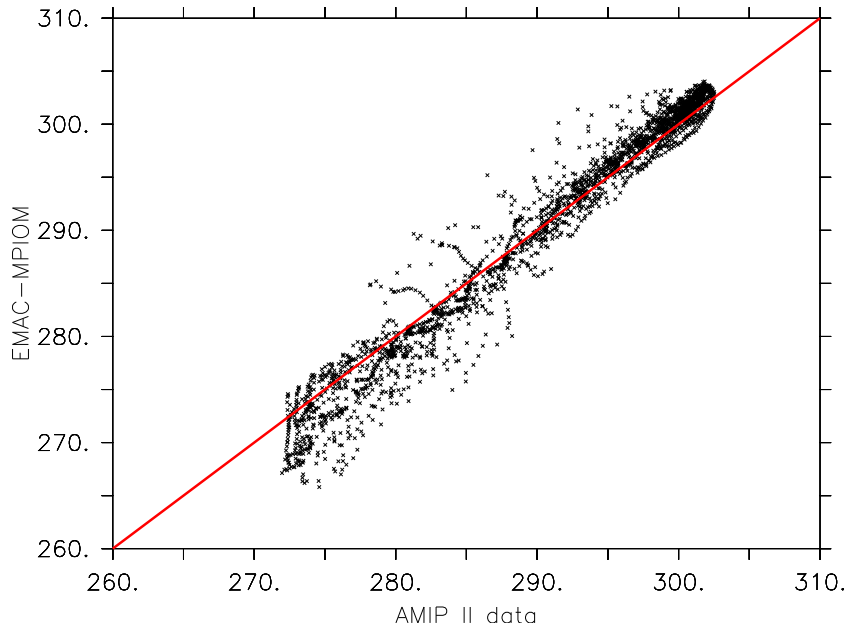

Fig. 5. Scatter plot of 1960–1990 average sea surface temperatures from the Taylor et al. (2000) dataset versus those resulting from simulation TRANS (in K).

GMDD
4, 457–495, 2011

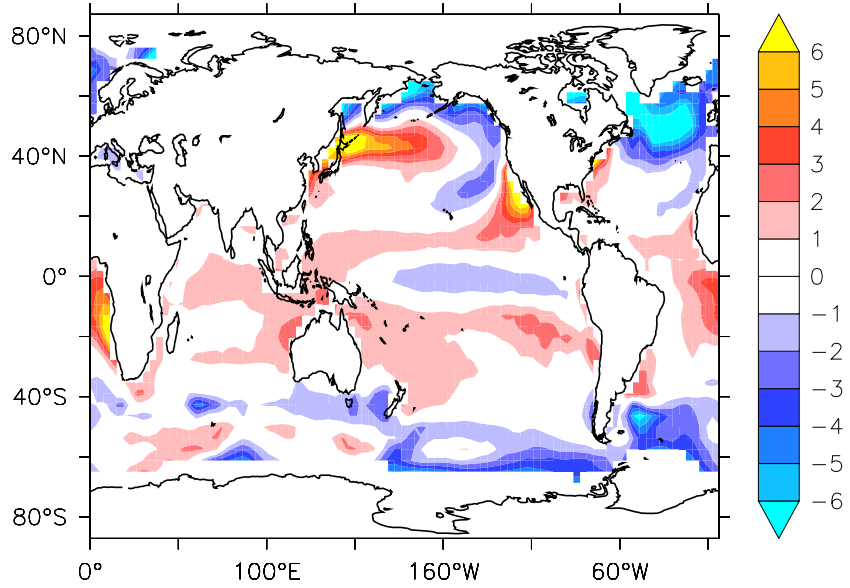

Fig. 6. Surface temperature differences between the AMIPII (Taylor et al., 2000) dataset and the simulation TRANS (in K). Both data have been averaged over the years 1960–1990.

GMDD
4, 457–495, 2011

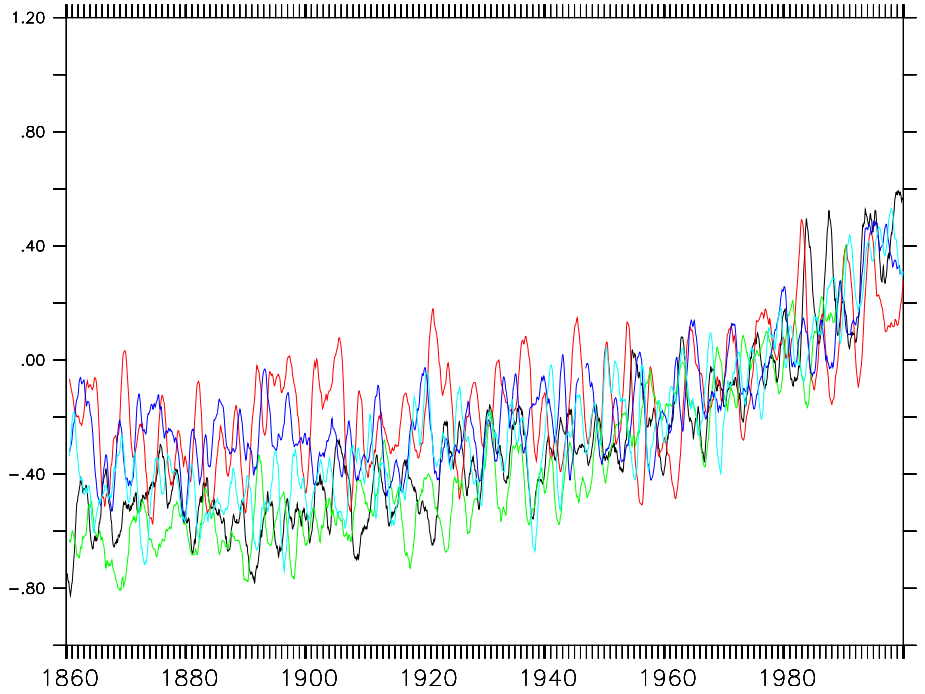

Fig. 7. Global surface temperature anomaly with respect to the 1960–1990 average in K. The lines represent a yearly running mean from simulation TRANS (black) and other IPCC AR4 models (20th century simulations; red: ECHAM5/MPIOM, green: INGV-SXG, blue: UKMO-HadCM3, light blue: IPSL-CM4).

GMDD
4, 457–495, 2011

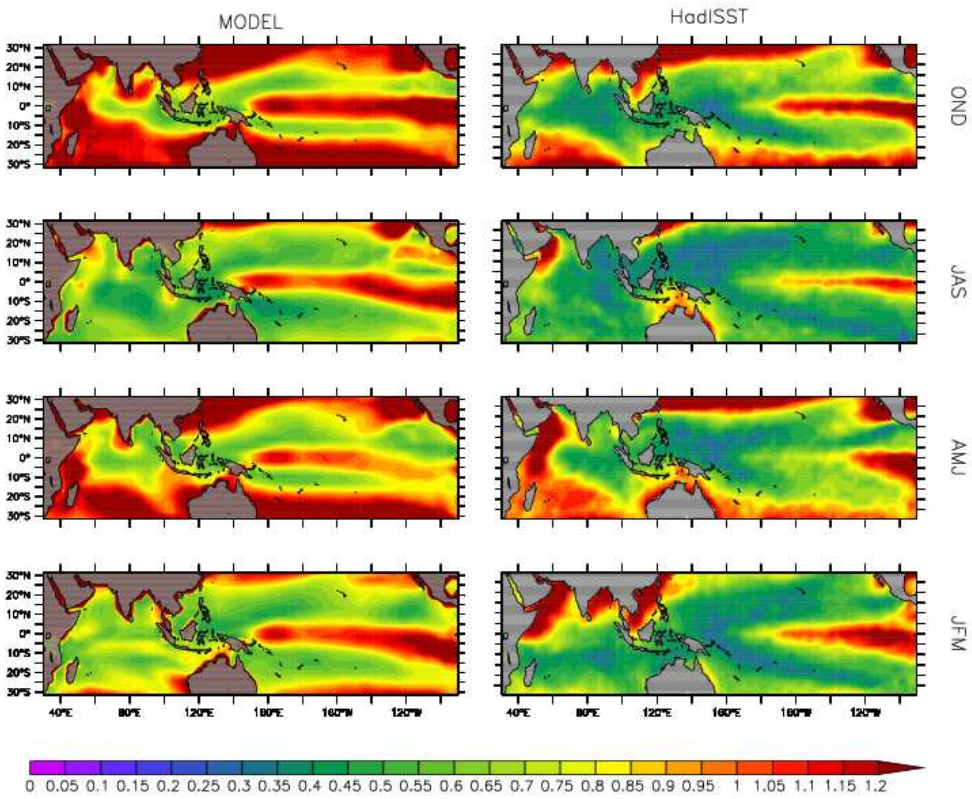

Fig. 8a. Standard deviation of the seasonal mean interannual variability of the SST (in K). The left and right columns show results from the TRANS simulation, and from the HadISST data (Rayner et al., 2003), respectively, both for the year 1900–1999 (not detrended).

GMDD
4, 457–495, 2011

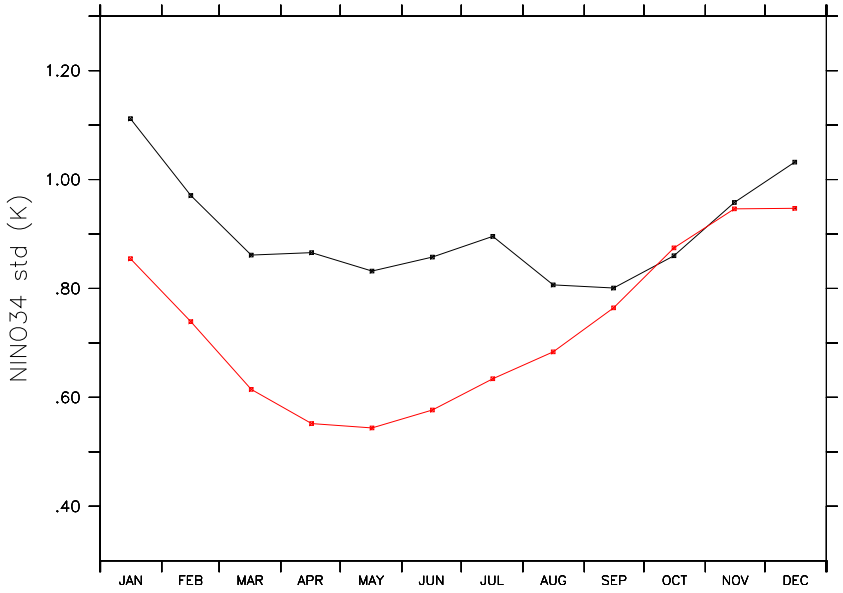

Fig. 8b. Standard deviation of monthly mean interannual variability of the SST (in K) averaged over the NINO3.4 region. The black line shows results from the PI simulation, and the red line from the HadISST data (Rayner et al., 2003), both for the year 1900–1999 (not detrended).

GMDD
4, 457–495, 2011

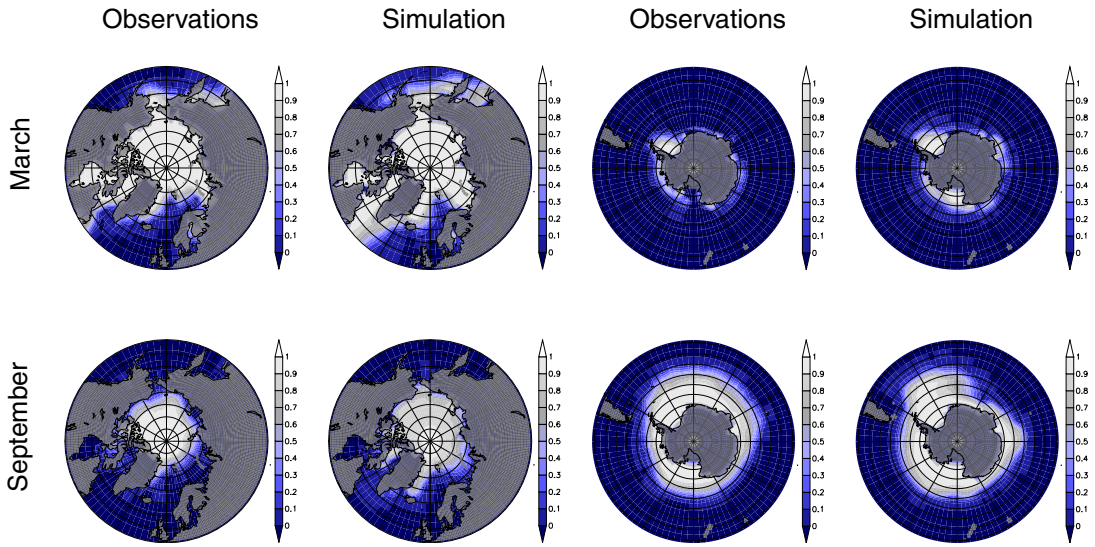

Fig. 9. Simulated and observed polar ice coverage. The upper and lower rows show March and September, respectively. Observations and results from simulation TRANS are averaged for the years 1960–1990. Observations are from the HadISST (Rayner et al., 2003) data set.

GMDD
4, 457–495, 2011

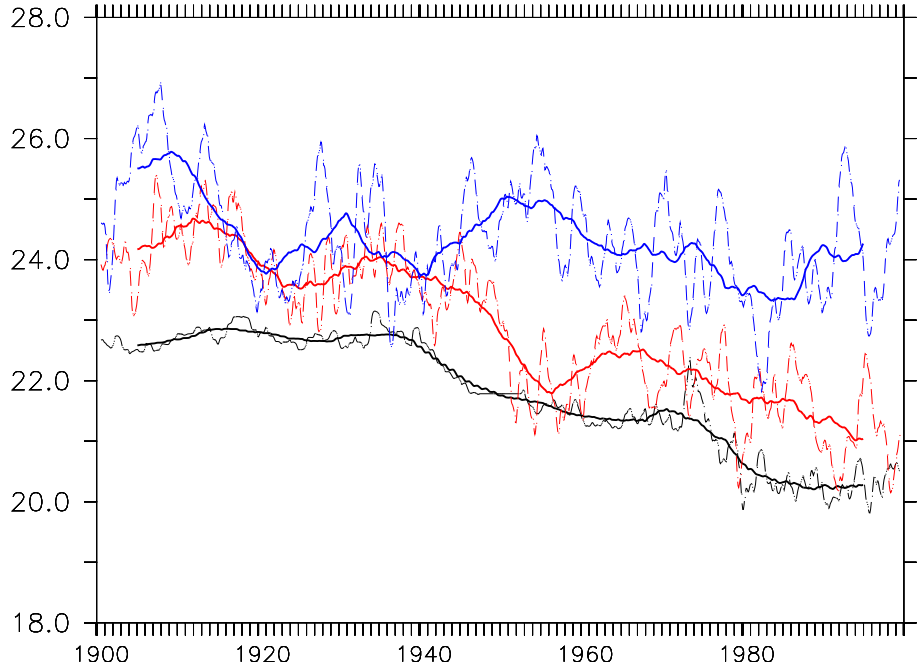

Fig. 10. Global sea ice coverage (in 10^{12} m^2). The black line shows the HadISST (Rayner et al., 2003) data, while the blue and the red lines represent the model results from simulations PI and TRANS, respectively. Dashed and solid lines represent annual and decadal running means, respectively.

GMDD
4, 457–495, 2011

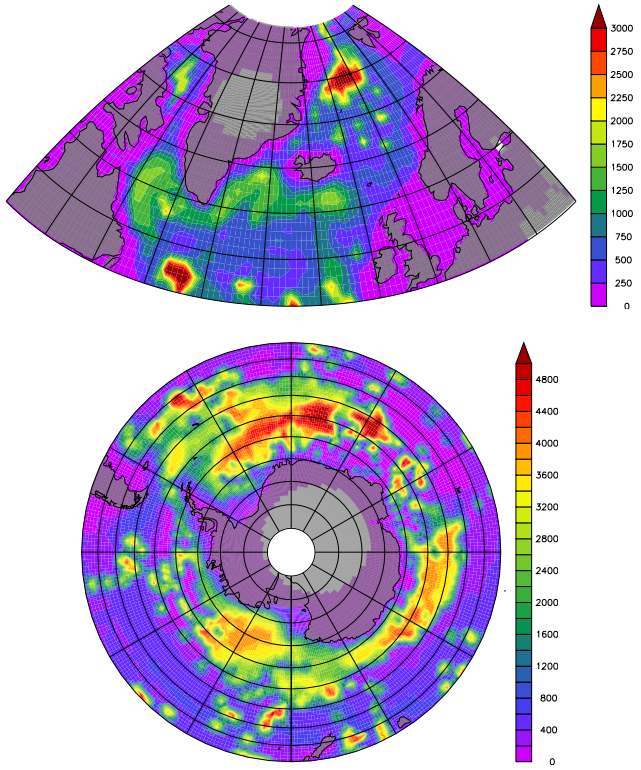

Fig. 11. Maximum depth (m) of vertical convection during the first 50 yr of simulation TRANS.

GMDD
4, 457–495, 2011

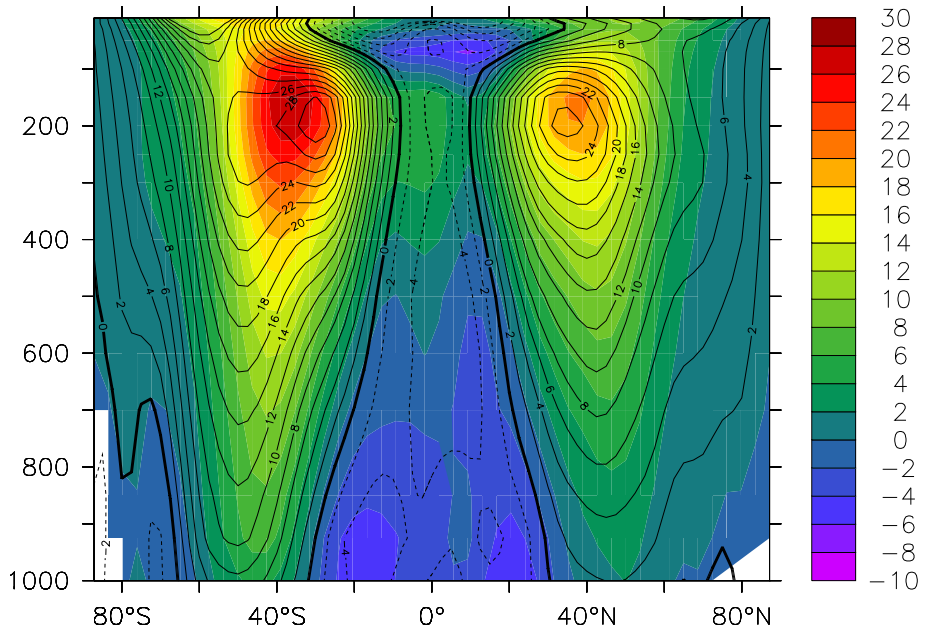

Fig. 12. Climatologically averaged zonal wind. The color denotes the wind speed in $m\,s^{-1}$ as calculated from simulation PI for the years 1950–2000, while the contour lines denote the wind speed calculated from the NCEP/NCAR Reanalysis 1 for the years 1968–1996. The vertical axis is in hPa.

GMDD
4, 457–495, 2011

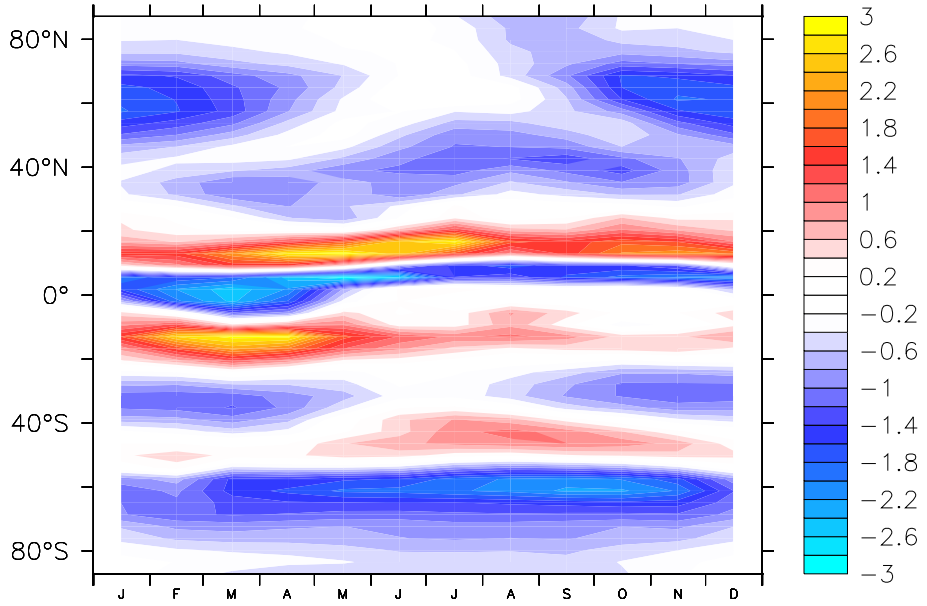

Fig. 13. Zonally averaged difference in the precipitation rate (in mm day^{-1}) between climatologies derived from simulation PI (1950–2000) and from observations (Global Precipitation Climatology Project, 1979–2009, Adler et al., 2003).

GMDD
4, 457–495, 2011

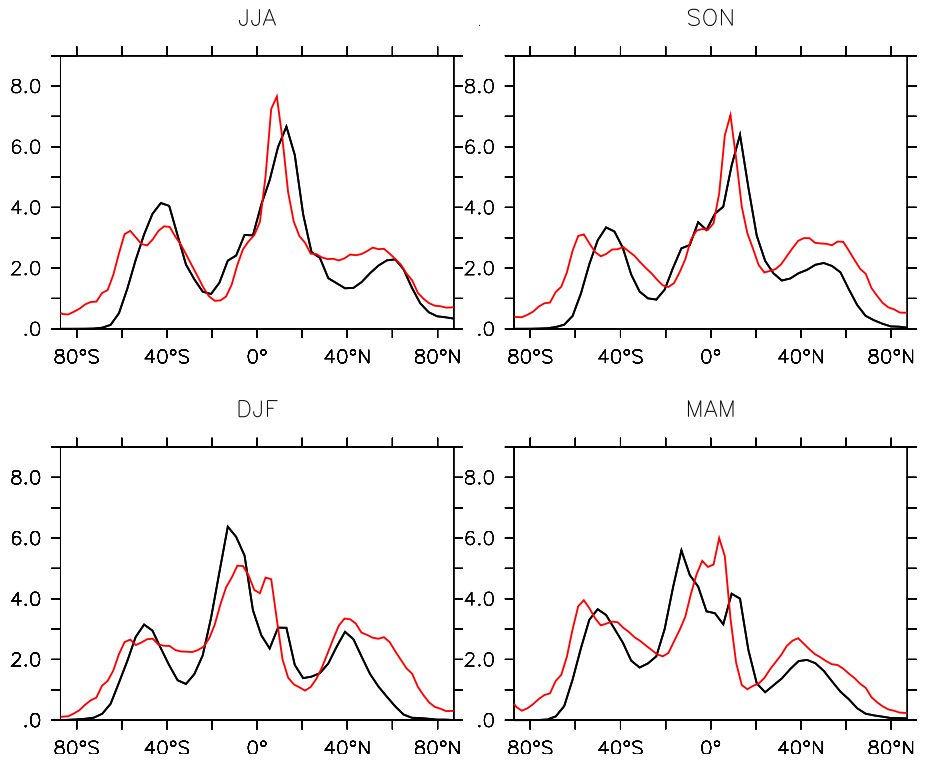

Fig. 14. Seasonal zonal average of climatological precipitation rate (in mm day^{-1}). The red lines show observations from the Global Precipitation Climatology Project (1979–2009 climatology), the black lines represent results from the simulation PI (1950–2000 climatology).

GMDD
4, 457–495, 2011